FOREX Publication
Open Access | Rapid and quality publishing

International Journal of
Electrical and Electronics Research (IJEER)
Research Article | Volume 14, Issue 3 | Pages 852-862 | e-ISSN: 2347-470X

Development of a Low-Cost Automated Papanicolaou Slide Stainer with Preliminary Image-Based Cellular Localization

Keeradit Saipattalung[1], SuraseePrahmkaew[2] and PasuraAungkulanon[3]
[1]*Faculty of Industrial Technology, Phranakhon Rajabhat University, Bangkok, Thailand; Email: keeradit@pnru.ac.th*
[2]*Faculty of Industrial Technology, Phranakhon Rajabhat University, Bangkok, Thailand; Email: surasee.p@pnru.ac.th*
[3]*Faculty of Engineering, King Mongkut's University of Technology North Bangkok, Bangkok, Thailand; Email: pasura.a@eng.kmutnb.ac.th*

***Correspondence:** *pasura.a@eng.kmutnb.ac.th*

ABSTRACT- This study developed and evaluated a low-cost automated Papanicolaou slide stainer integrated with a preliminary image-processing module for localizing suspicious cellular regions. The prototype used a Raspberry Pi 4 to control three-axis stepper motors, a servo-driven slide-rack gripper, and a 5-inch touchscreen. Its aluminum-profile structure accommodated nine reagent jars and up to ten slides per cycle, although two slides per cycle were used during prototype testing. In ten experimental cycles, touchscreen start, stop, and position-selection commands achieved 100% success, while the automatic staining sequence achieved 90%. The X-axis operated successfully in all trials, whereas the Y- and Z-axes each achieved 90% success. The mean staining time was 67.04 min per cycle. The prototype's staining quality received an overall mean score of 4.38 from expert evaluators. The image-processing workflow employed contrast enhancement, adaptive thresholding, watershed segmentation, and morphological feature extraction. Evaluation using 120 test images yielded an accuracy of 81.67%, sensitivity of 79.17%, specificity of 83.33%, precision of 76.00%, and F1-score of 77.55%. The prototype cost was approximately USD 780, substantially lower than that of an imported commercial slide stainer, and its break-even point was estimated at 76 tests, and 79 tests when maintenance costs were included. The findings support preliminary engineering and economic feasibility under the reported prototype conditions. The staining-quality score provides descriptive evidence only, and the localization metrics represent internal image-level agreement. Full-load endurance testing and external clinical validation remain necessary before routine laboratory application.

Keywords: Development, Evaluation, Low-Cost Medical Technology, Papanicolaou Staining, Image Processing, Break-Even Point.

ARTICLE INFORMATION

Author(s): Keeradit Saipattalung, Surasee Prahmkaew, and Pasura Aungkulanon;

Received: 24/05/26; **Accepted**: 27/09/26; **Published**: 30/09/26;
E- ISSN: 2347-470X;
Paper Id: IJEER 2405B15;
Citation: 10.37391/ijeer.140319
Webpage-link:
https://ijeer.forexjournal.co.in/archive/volume-14/ijeer-140319.html

Publisher's Note: FOREX Publication stays neutral with regard to jurisdictional claims in Published maps and institutional affiliations.

1. INTRODUCTION

Automation, machine vision, and image processing technologies are widely used in the industrial sector to enhance production efficiency, control quality, and reduce human error. [1] Use of the above technologies later expanded to have applications in security, robotics, agriculture, medicine, and quality control, such as computer vision monitoring systems [2], robotic navigation [3], machine learning and image processing applications in security work [4], image processing in Thailand's agricultural sector [5], the use of deep learning for agricultural image analysis [6], plant disease detection with image processing techniques [7], medical use of robotics [8], [9], automatic product sorting with image processing [10], fruit ripeness categorization [11], [12], detection of flaws on fabric [13], [14], signature authentication [15], and detection of printed circuit board flaws. [16] Evidence from these studies reflects how image analysis can effectively support detection of anomalies, model categorization, and decision-making in processes that need high accuracy. In pathology and cytology, slide preparation and sample staining quality are key factors for interpretation accuracy because the clarity of nuclei, cytoplasm, and cell morphology characteristics is baseline data used by experts in diagnoses. [17] The Papanicolaou staining method is a standard technique based on a study conducted by Papanicolaou and Traut [18] used in cytological examinations, particularly in screening cervical cells for anomalies. Later, cytopathological knowledge was systematically developed and summarized in standard textbooks, such as Koss' Diagnostic Cytology and Its Histopathologic Bases, which emphasized the importance of sample preparation and cytological interpretation quality. [19] Nevertheless, the abovementioned staining process requires control over multiple variables, such as sample fixation time, order of fixation, staining time, cleaning, and contamination prevention. Operator error may

FOREX Publication
Open Access | Rapid and quality publishing
International Journal of Electrical and Electronics Research (IJEER)
Research Article | Volume 14, Issue 3 | Pages 852-862 | e-ISSN: 2347-470X

affect dye quality and slide consistency [20]. Although an automated slide stainer can improve slide preparation standards, many commercial instruments are expensive, dependent on imports, and carry maintenance costs, making access difficult for medium-sized laboratories or service venues with limited resources. Therefore, studies have been conducted with an aim to develop low-cost laboratory instruments, such as corrosion-resistant multitasking cell stainers [21], cost-effective automated cytological slide reading platforms [22], and automated modular and open-source slide scanning microscopes for areas with limited resources. [23] These studies indicate the feasibility of developing low-cost equipment capable of supporting cytological work. In Thailand, cancer remains a major public health problem, and data from the nation's oncological units reflect the need for accessible and effective screening systems suitable for healthcare facility contexts. [24] A review of slide-staining systems and related studies found that commercial slide stainers could effectively control the staining process but were costly. In contrast, most low-cost prototypes developed in previous studies primarily focused on mechanical systems and motion control. However, they remained limited in integrating Papanicolaou staining, automated control, and image analysis into a single system. Therefore, this study aimed to develop a low-cost Papanicolaou staining method slide stainer with a basic system for locating cellular anomalies from digital microscope images with a goal to reduce chemical exposure among operators, reduce instrument procurement costs, and support screening. The image processing system in this study has a purpose to help locate suspicious positions and areas for subsequent consideration by experts with no objective to replace clinical diagnosis by a doctor or cytotechnologist. The engineering novelty of this work consisted of (1) the integration of an automated nine-jar Papanicolaou staining machine, a 3-axis motion system, and a 3D-printed rack-gripping assembly into a low-cost prototype, (2)a touchscreen-based user interface that supported both automatic and semi-automatic modes, and (3) an explainable image-processing module that used morphological criteria to flag regions warranting re-examination, positioned as a preliminary screening aid rather than a diagnostic system. This work therefore aimed to fill the gap between low-cost staining machines that focused solely on mechanical function and imaging systems that had not integrated the staining sequence into the same platform. The related work comparison was as shown in *table 1*.

2. RELEVANT LITERATURE

Cytological and tissue sample staining is an important process that helps to enhance differences of components within cells for clearer observation of morphological characteristics. In this study, the researcher emphasized sample slides for cytological work entered the Papanicolaou staining process, a standard method widely used in basic screening and diagnostic work, as shown in *figure 1*.

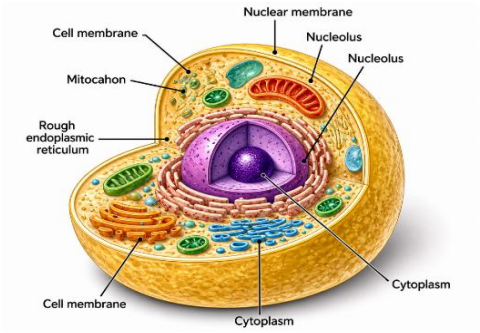


Figure 1. The nucleus of a cell [Online Source: http://www.digitalschool.club/]

Staining can be classified into three main groups [25] as follows: (1) vital staining for living organisms or cells; (2) routine staining, which is the standard staining in laboratories; and (3) special staining used to study special pathological characteristics, such as mold, bacteria, or substances created by cells. Papanicolaou stain is classed as routine staining used mainly in clinical cytology. [26] In this method, hematoxylin is used for staining nuclei and Orange G (OG-6) is used with Eosin Azure (EA-50) to show cytoplasm details, allowing differences between normal and anomalous cells to be clearly distinguished. [27].

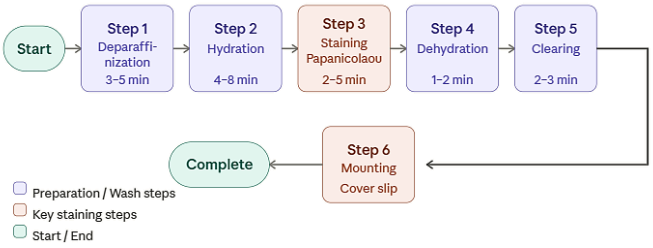


Figure 2. The Papanicolaou staining procedure for tissue samples

The processes of Papanicolaou staining shown in *figure 2* are as follows:

Step 1: Deparaffinization is the process of melting wax medium from tissue slides with xylene before dying, because the wax would coat cells and tissues to prevent staining, which takes 3-5 minutes per container. However, in Papanicolaou's method for direct smear, this step can be skipped if the slide has not undergone paraffinization.

Step 2: Hydration is the process of cleaning xylene from tissues and preparing slides for dye fixation by using ethyl alcohol at concentrations of 100%, 95%, and 70%, respectively, to reduce concentrations to appropriate conditions for approximately 1-2 minutes per container or a total of 4-8 minutes.

Step 3: Staining is the main staining process using Papanicolaou's method in three sub-steps, consisting of staining with hematoxylin to show nuclei, followed by bluing with water or an ammonia medium, and continued staining

FOREX Publication
Open Access | Rapid and quality publishing
International Journal of Electrical and Electronics Research (IJEER)
Research Article | Volume 14, Issue 3 | Pages 852-862 | e-ISSN: 2347-470X

with Orange G and Eosin Azure to show cytoplasm structures. Each sub-step of staining took 2-5 minutes, depending on medium concentration and temperature.

Step 4: Dehydration is the process of extracting water from slides before clearing. This step is done using 95% and 100% ethyl alcohol, respectively, and took 1-2 minutes per container.

Step 5: Clearing is the process of making slides free of bubbles and preparing slides for transparent coating by using a xylene medium. This step took 2-3 minutes.

Step 6: Mounting is the step of coating glass slides with a mounting medium to preserve tissues and facilitate clear microscopic examination.

Table1. Comparison of Related Work with the Proposed System

System/ Source	Main Task	Control/ Structure	Through-put	Image Analysis	Cost/ Limitations
Liao et al. [21]	Automated cell staining	Corrosion resistant mechanism	Not reported	None	No image analysis
Ocampo-López-Escalera et al. [22]	Cervical slide imaging	Low-cost automated scanner	Scanner-dependent	Available	Did not integrate Pap staining
Lu et al. [23]	Automated slidescanning	Open-source three-axis system	Scan-area dependent	Image acquisition	No staining module
Ponzetti et al. [28]	Automated Slidestaining	Modified 3D printer	Not reported	None	No Pap-specific image analysis
Proposed system	Pap staining and suspicious-region localization	Raspberry Pi 4, three-axis motion, and nine jars	Up to 10 slides/ cycle	Training-free, explainable morphology-based localization	USD 780; internal 120-image test; no external validation

Table 1 presents a functional benchmark of the systems. The automated stainers in studies [21] and [28] control the staining process but lack image-analysis capabilities. In contrast, the low-cost cervical cytology platform in [22] and the open-source scanner in [23] support image acquisition or analysis but do not integrate the nine-jar Papanicolaou staining procedure. Compared with the deep-learning microscopic-image classification approach in [17], the proposed workflow requires no model-training dataset and uses explicit, traceable morphological rules. However, accuracy values cannot be directly compared across these studies because their objectives, specimens, datasets, and imaging conditions differ.

3. DESIGN AND DEVELOPMENT OF THE LOW-COST SLIDE STAINER

Development of the system in this study was composed of two main parts: (1) design and production of the low-cost automated slide stainer for the Papanicolaou staining process; and (2) preparation for analysis of basic digital microscope images after staining. Control of the system uses Raspberry Pi4 as the central processing unit in controlling stepping motors for movements along the X, Y, and Z axes and in controlling the servomotor for picking up slide racks. The abovementioned design is aimed at reducing stainer costs and risk of repetition with chemicals.

3.1. Hardware Structural Design

In hardware structure design, the researcher uses Raspberry Pi4 as the central processing unit and links to the 3-axis stepping motors, the servomotor, the touch screen display, and the miniature digital microscope. The system was designed to control movements of the slide rack gripper according to staining steps and support post-staining image capture for basic analysis and location of cellular anomalies as shown in *figure 3*.

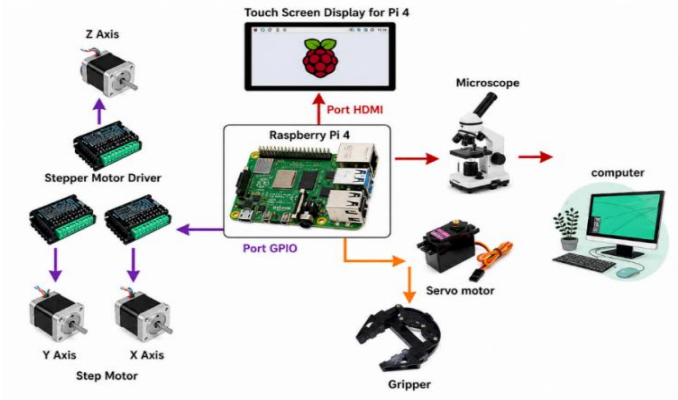


Figure 3. Hardware structure design

From *figure 3*, the hardware structural design has a Raspberry Pi 4 board as the central processing unit performing control functions. The touch screen display shows results and orders all three stepping motors and the gripper to work after tissue staining. In addition, the design features connections to the miniature microscope for tissue image processing after staining. Image processing analyzes for anomalous points for basic disease analysis.

3.2. Software Design

The software was divided into 4 layers: (1) the user interface layer, which received Start, Stop, Home commands and jar position selections via the touchscreen; (2) the task sequence control layer, which managed the HOME–MOVE–DIP–DWELL–LIFT–NEXT–FINISH states while monitoring for emergency stop commands; (3) the device control layer, which converted jar coordinates into stepping motor pulse counts and issued PWM signals to the servo motor; and (4) the image processing layer, which received images from the digital microscope, processed them, and saved the images with marked regions.

The system communicated with the stepper motor drivers through the Raspberry Pi 4 GPIO interface and connected to the digital microscope via USB. The prototype software was developed in Python 3.9.2 on Raspberry Pi OS Bullseye 64-bit.

FOREX Publication
Open Access | Rapid and quality publishing
International Journal of Electrical and Electronics Research (IJEER)
Research Article | Volume 14, Issue 3 | Pages 852-862 | e-ISSN: 2347-470X

OpenCV 4.5.5 and NumPy 1.19.5 were used for image acquisition, enhancement, segmentation, feature extraction, and suspicious-region localization. Images were captured at 1,920 × 1,080 pixels under controlled illumination and fixed-magnification conditions.

The control sequence calculated position from *equation (1)*, where s was the distance traveled (millimeters), n_p was the number of pulses, N_s was the number of steps per revolution, m was the micro step value, and L was the distance traveled per revolution of the transmission assembly. The total cycle time was calculated from *equation (2)*. The HOME coordinate values and the center position of each jar were calibrated before testing by moving step-by-step and recording the number of pulses that positioned the rack at the center of the jar.

$$s = n_p/(N_s m) \times L \quad (1)$$

$$T_{total} = \Sigma\left(t_{move}, i + t_{dip}, i + t_{dwell}, i + t_{lift}, i\right) for \text{jars} i = 1, \ldots, 9 \quad (2)$$

Process procedures of the system: (1) initialized the GPIO, camera, and display; (2) homed all three axes; (3) received commands and checked the Stop status; (4) for jars 1–9, moved to the coordinate, raised/lowered the rack the specified number of times, paused for the specified duration, and recorded the status; (5) returned to Home; (6) captured the image after staining; (7) processed the image and displayed circled regions that met the suspicious criteria; (8) saved the results and finished. If a timeout occurred or a Stop command was received, the system halted the pulses, raised the rack to a safe position, and recorded an error code. The system's working structure is as shown in *figure 4.*

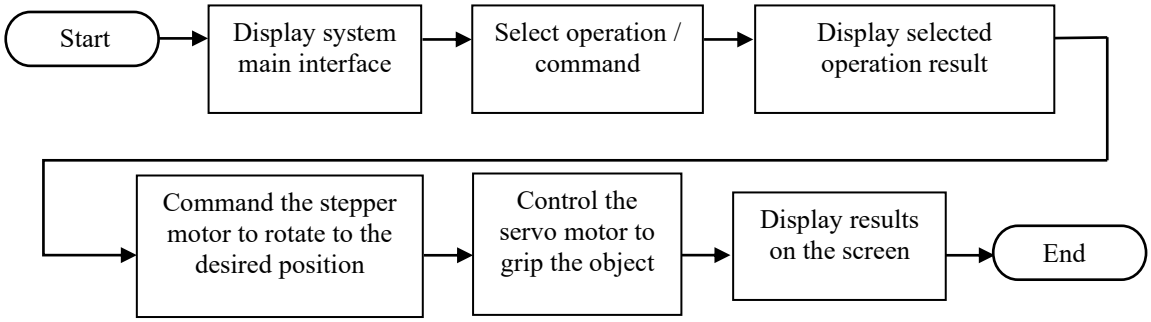
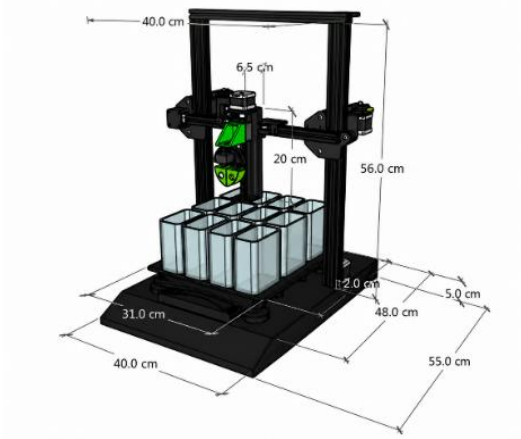


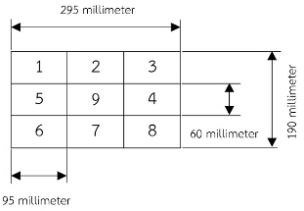
Figure 4. shows the program structure of the tissue staining machine

3.3. Stainer Structure Design

The stainer's structure is made from 20 x 20-millimeter aluminum profiles with a width of 40.0 centimeters, a length of 55.0 centimeters, and a height of 56.0 centimeters. The stainer was designed to support installation of a 3-axis motor system (X, Y, and Z axes) and nine chemical containers. The design was aimed at making the device compact and simple to maintain as shown in *figure 5(a).*



(a)



(b)

Figure 5. shows the structure of the staining machine and the placement of the glass jars

According to *figure 5(b),* the work piece base structure has dimensions of 190 millimeters in width x 295 millimeters in length, and the space for placing containers has dimensions of 60 millimeters in width x 95 millimeters in length. Nine container spaces are available with the following specifications for chemical containers: 1) 95% Ethanol; 2) 70% Ethanol; 3) Hematoxylin; 4) Distilled Water; 5) OG-6 (Orange G); 6) EA-50; 7) Absolute 100% Alcohol; 8) Xylene; and 9) Empty Container.

3.4. Stainer Function Design

The slide stainer's functions are controlled via the function control display designed for semi-automatic and automatic use in order to allow users to issue "Start", "Stop", and "Select Position" commands. Automatic functions will follow the steps in *figure 6.*

FOREX Publication
Open Access | Rapid and quality publishing
International Journal of Electrical and Electronics Research (IJEER)
Research Article | Volume 14, Issue 3 | Pages 852-862 | e-ISSN: 2347-470X

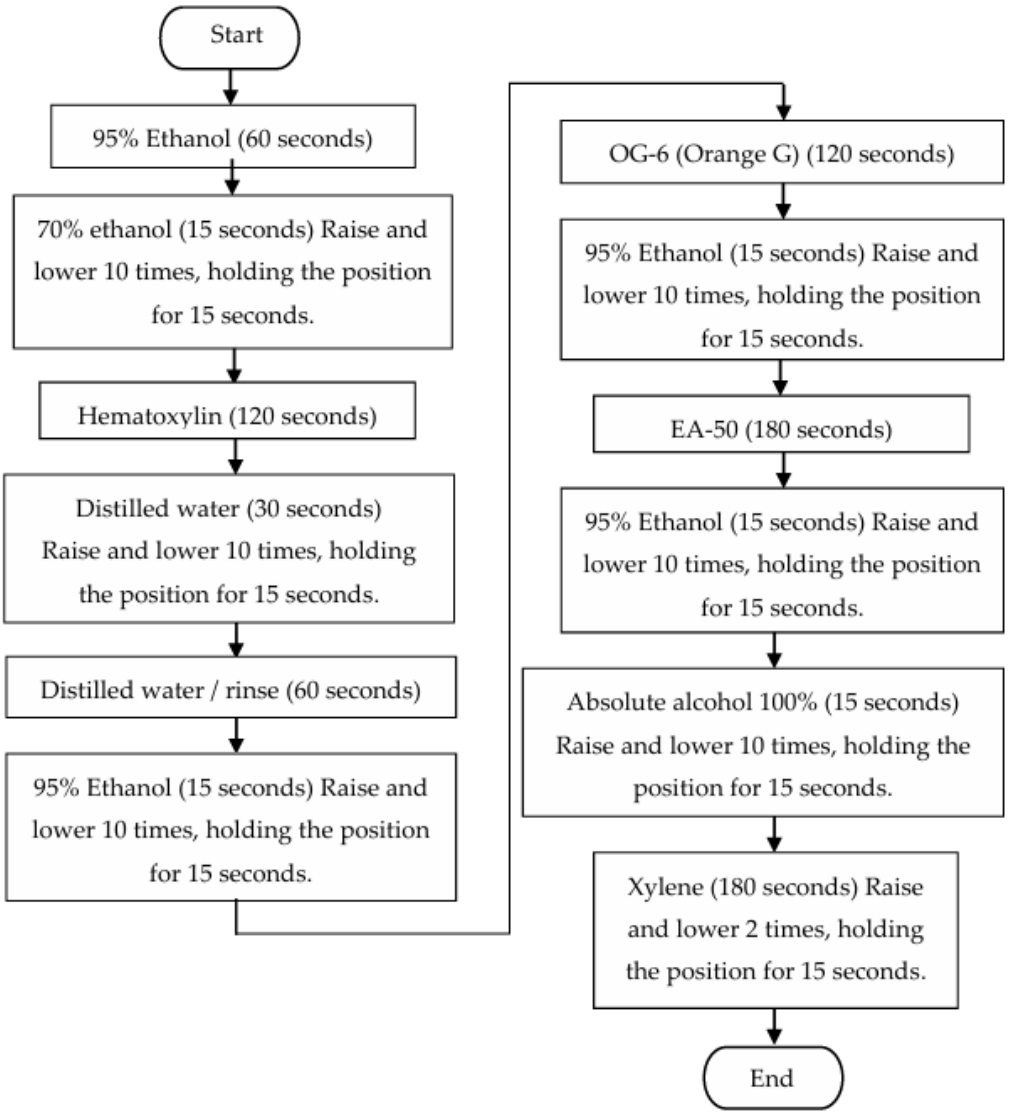


Figure 6. Sequence of Papanicolaou staining

3.5. Criteria for Identifying Suspicious Regions Using Image Processing

The localization algorithm was implemented in Python 3.9.2 using OpenCV 4.5.5 and NumPy 1.19.5. All images were acquired at 1,920 × 1,080 pixels using the same microscope magnification and illumination. The reproducible processing sequence was as follows: (1) convert the RGB image to CIELAB, apply CLAHE to the L channel (clipLimit = 2.0; tileGridSize = 8 × 8), and convert the enhanced image to grayscale; (2) smooth the image with a 5×5 Gaussian kernel (σ = 0); (3) obtain a binary nuclear mask with adaptive Gaussian thresholding (blockSize = 31, C = 5, THRESH_BINARY_INV); (4) perform one morphological opening with a 3 × 3 elliptical kernel and two closings with a 5 × 5 elliptical kernel; (5) discard connected components smaller than 50 pixels or larger than 5,000 pixels; and (6) separate touching nuclei using the L2 distance transform (mask size = 5), with sure foreground defined as values ≥ 0.40 of the maximum distance in each component, followed by marker-controlled watershed segmentation.

For each segmented nucleus, nuclear area (A_n), perimeter (P), circularity ($C = 4\pi A_n/P^2$), and mean nuclear darkness (I_n = 255 minus the mean grayscale intensity) were calculated. The candidate cell region was obtained by seed-based region expansion from the nucleus, limited to a 40-pixel radius and to pixels with HSV saturation ≥ 20 and value ≤ 245; its area was denoted by Ac. The nuclear-to-cell ratio was $N/C = A_n/Ac$. Local density (D) was the number of nuclear centroids within a 100-pixel radius divided by the circular neighborhood area.; and the suspicion score is as shown in *equation (3)*.

$$S = w_1 z(A_n) + w_2 z(N/C) + w_3 z(I_n) + w_4 z(1 - C) + w^5 z(D) \quad (3)$$

where I_n was the nucleus intensity, D was the local density, z(.) represented feature standardization, and ω_i represented the corresponding feature weights. The system marked a region as potentially suspicious when $S \geq \tau$ or when the region satisfied at least two of the key criteria presented in *table 2*.

Table 2. Preliminary Criteria for Identifying Suspicious Regions Using Image Processing

Feature	Evaluation Method	Preliminary Warning Criterion

FOREX Publication
Open Access | Rapid and quality publishing
International Journal of Electrical and Electronics Research (IJEER)
Research Article | Volume 14, Issue 3 | Pages 852-862 | e-ISSN: 2347-470X

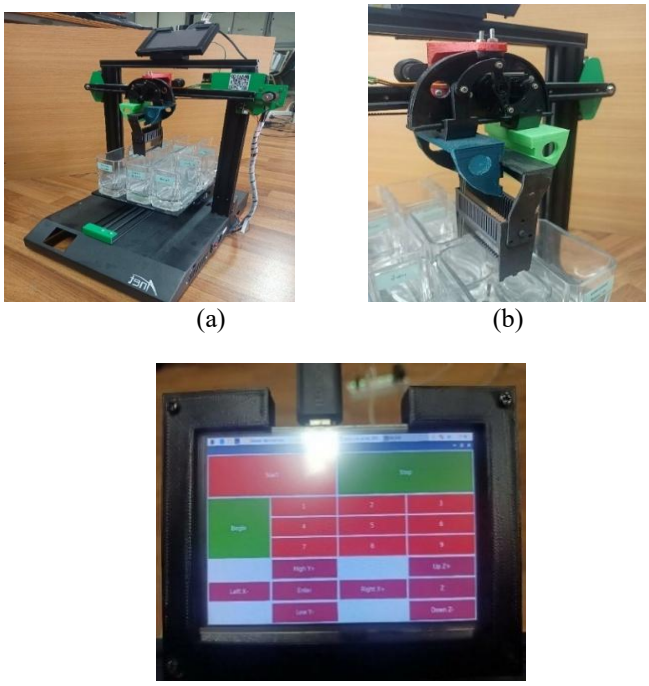
Nuclear size	A_n: pixel area of the watershed nucleus	$A_n \geq 1.5 \times$ the within-image median A_n; relative limit selected to identify nuclear enlargement while reducing scale dependence.
N/C ratio	$N/C = A_n/Ac$	$N/C \geq 0.40$; morphology-based screening limit supported by cytological characteristics in [19].
Nuclear darkness	$I_n = 255 -$ mean grayscale intensity	$I_n \geq$ median(I_n) + 1.0 × 1.4826MAD(I_n); robust within-image limit for hyperchromatic nuclei.
Nuclear shape	$C = 4\pi A_n/P^2$	$C < 0.75$; fixed limit for loss of circularity or an irregular nuclear boundary.
Size variation	A_n divided by the median A_n of nuclei within 100 pixels	Local size ratio ≥ 1.5; relative limit for anisokaryosis.
Clustering/overlap	Count of nuclear centroids within 50 pixels	At least 3 nuclei; fixed rule for a compact or overlapping cluster.
Local density	D: centroids within a 100-pixel radius divided by neighborhood area	D ≥ 2.0 × the within-image median D; relative limit for hypercellular regions.

The conditions presented in *table 2* serve as preliminary engineering screening criteria based on cellular morphological characteristics reported in the literature [19] and preliminary testing of the developed system. Fixed thresholds, including an N/C ratio of ≥ 0.40, circularity of < 0.75, and clusters of at least three nuclei, identify nuclear enlargement, shape irregularity, and cellular overlap. Relative thresholds, including a nuclear size of at least 1.5 times the within-image median and a local density of at least 2.0 times the median, reduce the effects of variations in magnification, staining intensity, and illumination. The system identifies a region as suspicious when its score is S ≥ 1.50 or when it satisfies at least two primary criteria. These engineering criteria support preliminary localization only and do not constitute clinical diagnostic criteria.

4. PROTOTYPE SLIDE STAINER AND BASIC CELLULAR ANOMALY LOCATING SYSTEM TEST

4.1. Tissue Slide Stainer Production Results

The prototype was manufactured according to specified dimensions and characteristics, consisting of the main structure, the 3-axis motor, the 3D-printed slide rack gripper, servomotors for gripping, and the touch screen display for commands as shown in *figure 7(a)-(c)*. The abovementioned component arrangement enabled users to prepare samples, order staining to begin, and monitor system status more conveniently.



(a) (b) (c)

Figure 7. Prototype of a low-cost slide staining and tissue analysis machine using the Papanicolaou Staining Method.

According to *figure 7(a)*, the prototype low-cost slide stainer and tissue analysis device using the Papanicolaou method was assembled as designed in black and installed with a touch screen display, handles, and glass chemical containers. *Figure 7(b)* shows a 3D-printed slide rack gripper fitting the finished handles and *figure 7(c)* shows the slide stainer control display.

4.2. Control System Testing Results

From testing for ten rounds, the system was found to be able to start and stop functions via the touch screen display every time. The system responded to initial commands accurately for ten times (100%) and stopped functions according to commands accurately for ten times (100%). This showed the system controlled with Raspberry Pi and a touch screen display was able to function with stability within the prototype's scope as shown in *table 3*.

Table 3. Testing the functionality of the control system

Test Item	Number of Tests	Number of Successes	Percentage
Starting operation via touchscreen	10	10	100.00
Stopping operation via touchscreen	10	10	100.00
Selecting operating position	10	10	100.00
Operating according to automatic program sequence	10	9	90.00

According to *table 3*, functions according to automated program sequences were successful for 9 times out of 10 times or 90.00% with one error found due to the gripper stalling

FOREX Publication
Open Access | Rapid and quality publishing
International Journal of Electrical and Electronics Research (IJEER)
Research Article | Volume 14, Issue 3 | Pages 852-862 | e-ISSN: 2347-470X

while moving along the Z axis. This result indicates the system has automated function capacity with need for improvements to mechanism reliability for a heavily loaded axis and vertical movement.

4.3. Axial Movement Test Results

Mechanical validation uses 10 repeated trials for each axis and the gripper. An axis trial is successful when the rack reaches the calibrated jar-center target without manual correction; a gripper trial is successful when the grip-lift-lower-release sequence finishes without a stall or dropped rack. Operational repeatability and reliability equal successful trials divided by total trials, and the error or failure rate equals unsuccessful trials divided by total trials. Two-sided 95% confidence intervals use the exact Clopper-Pearson method as shown in *table 4.*

Table 4. Quantitative Mechanical Validation of Axis Positioning and Gripper Operation.

Component	Trials	Passed	Failed	Reliability, % (95% CI)	Error rate (%)	Component
X-axis positioning	10	10	0	100.00 (69.15-100.00)	0.00	X-axis positioning
Y-axis positioning	10	9	1	90.00 (55.50-99.75)	10.00	Y-axis positioning
Z-axis positioning	10	9	1	90.00 (55.50-99.75)	10.00	Z-axis positioning
Gripper operation	10	9	1	90.00 (55.50-99.75)	10.00	Gripper operation

According to *table 4*, the *X*-axis achieves 100.00% repeatability and reliability (10/10), whereas the Y-axis and Z-axis each achieve 90.00% (9/10). The gripper also achieves 90.00% operational reliability (9/10), with one stall during Z-axis movement. The exact confidence intervals remain wide because each component has only 10 trials. Therefore, the results support preliminary mechanical reliability but do not establish absolute positioning accuracy because endpoint displacement in millimeters is not recorded.

4.4. System Work Time Test Results

The repeated-cycle evaluation uses two slides per cycle and the fixed nine-jar Papanicolaou program. Each run applies the same programmed movement, dipping, dwell, and return-to-home sequence. The system records the elapsed time and whether the automatic sequence finishes without mechanical interruption, from testing for 10 rounds were as shown in *table 5.*

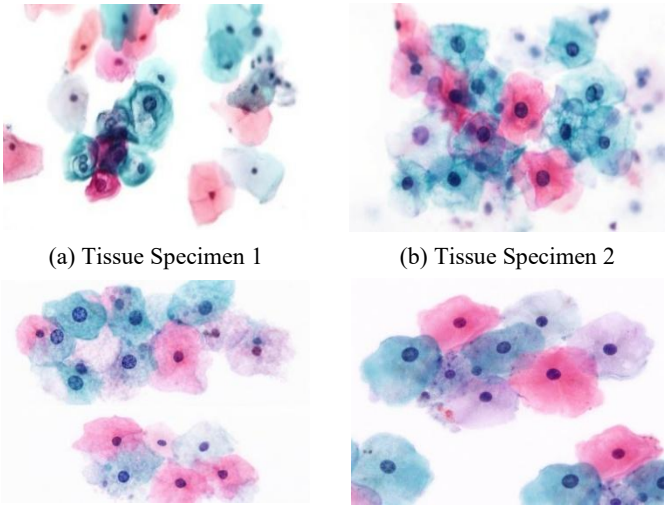
Table 5. System-wide runtime testing.

No	x_i (minutes)	$x_i - \bar{x}$	$(x_i - \bar{x})$	No	x_i (minutes)	$x_i - \bar{x}$	$(x_i - \bar{x})^2$
1	67.20	0.16	0.0256	6	66.95	-0.09	0.0081
2	66.85	-0.19	0.0361	7	67.10	0.06	0.0036
3	67.05	0.01	0.0001	8	66.80	-0.24	0.0576
4	66.90	-0.14	0.0196	9	67.25	0.21	0.0441
5	67.30	0.26	0.0676	10	67.00	-0.04	0.0016
				Average	67.04		0.0264

According to *table 5*, 10 full cycles, the system accumulates 670.40 min (11.17 h) of operation. Cycle time ranges from 66.80 to 67.30 min, with a mean of 67.04 min, an SD of 0.17 min, and a coefficient of variation of 0.25%. The automatic sequence completes without error in 9 of 10 trials (90.00%); one trial records a gripper stall during Z-axis movement. These results show short-term repeatability under the stated prototype conditions.

4.5. Slide Staining Results and Assistance in Basic Cellular Anomaly Location

From testing slide stainer functions in the staining process, mean working time for one round was found to be 67 minutes. In this prototype testing, the researcher used two sample slides per time. When the user pressed “Start” on the command display, the system began the staining sequence according to specified steps automatically. Sample staining results were as shown in *figures 8(a) to 8(d).*



(a) Tissue Specimen 1 (b) Tissue Specimen 2

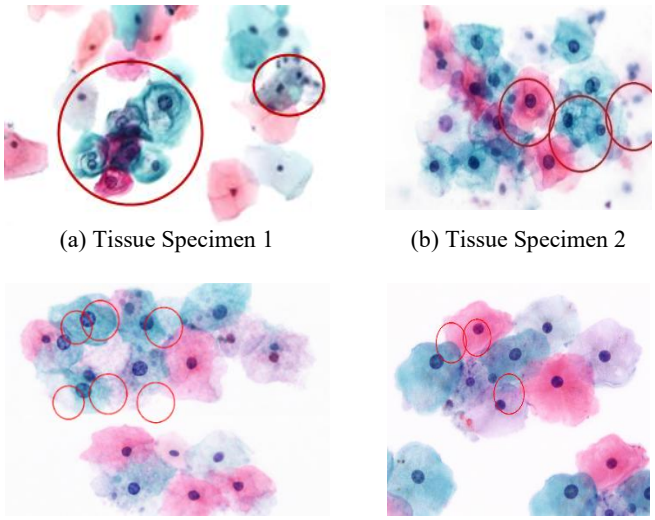
(c) Tissue Specimen 3 (d) Tissue Specimen 4

Figure 8. Results of tissue staining experiment.

According to *figure 8*, slides dyed by the Papanicolaou method can be visibly observed to have sample distribution on glass slides. However, cellular structure detail assessment remains

FOREX Publication
Open Access | Rapid and quality publishing
International Journal of Electrical and Electronics Research (IJEER)
Research Article | Volume 14, Issue 3 | Pages 852-862 | e-ISSN: 2347-470X

dependent on further assessment of digital microscope images. Therefore, this study used digital microscope images as input data for basic processing to identify positions requiring detailed consideration by experts as shown in *figure 9.*



(a) Tissue Specimen 1 (b) Tissue Specimen 2

(c) Tissue Specimen 3 (d) Tissue Specimen 4

Figure 9. Results of the analysis of the locations where cell abnormalities are likely to be present

According to *figure 9*, presents four representative examples of the regions marked by the system. These illustrations demonstrate the localization output only and do not represent independent clinical diagnoses. For the formal 120-image evaluation, the study compares the system outputs with the expert-consensus reference labels described.

4.6. Evaluation of Slide-Staining Quality

The slide-staining quality was evaluated in collaboration with the Anatomical Pathology Laboratory at Bhumibol Adulyadej Hospital, Directorate of Medical Services, Royal Thai Air Force. The evaluation covered five aspects: nuclear clarity, cytoplasmic color differentiation, staining uniformity, background artifacts, and the overall acceptability of the slides. The evaluation results are presented in *table 6.*

Table 6. Results of the Slide-Staining Quality Evaluation

Evaluation Aspec	Prototype Mean	SD	Standard Method Mean	SD
Nuclear clarity	4.42	0.52	4.59	0.51
Cytoplasmic colo differentiation	4.31	0.43	4.58	0.54
Staining uniformity	4.43	0.50	4.62	0.53
Background artifacts	4.37	0.44	4.61	0.53
Overall acceptability	4.41	0.51	4.68	0.52
Overall mean	4.38	0.48	4.62	0.53

Table 6 showed that the overall mean score for the slide-staining quality achieved by the prototype was 4.38, which was rated at a very good level. Meanwhile, the laboratory standard method obtained an overall mean score of 4.62, which was also rated at a very good level. These results indicated that the developed prototype achieved staining quality comparable to the standard method; however, further improvements were still required.

4.7. Slide Stainer Break-even Point Calculation Results

Development of the low-cost slide stainer in this study had a goal to reduce foreign slide stainer imports. Therefore, cost-efficiency considerations were based on analysis of the break-even point from fixed cost, cost fluctuation per time, and revenue per service. The break-even point is the number of times the machine must be used to recover all costs. At this point, the machine makes no profit and no loss. After this point, each additional use generates profit [29-30]. Based on an exchange rate of THB 32.947 per USD, the fixed cost of the main materials and equipment was approximately USD 781.56. The variable cost was USD 17.00 per operation, while the revenue was USD 27.32 per test. Therefore, the break-even point was calculated as follows:

$$N^* = \frac{F}{p - v} = \frac{25{,}750}{900\text{-}560} = 75.735 \text{ Time}$$

Where F is Fixed Cost, v is Variation of Cost per Unit, p is Price per Unit, and N* is Net Production at Break-even Point.

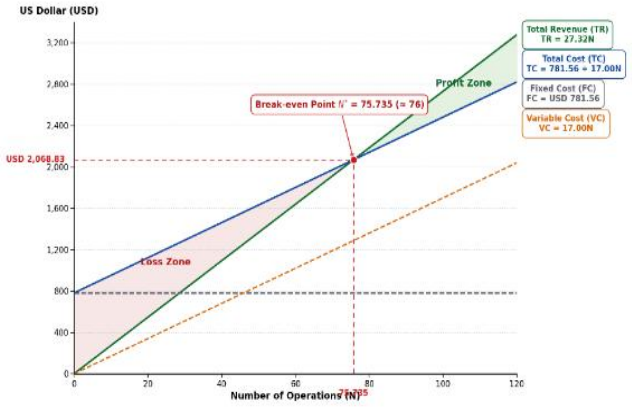


Figure 10. Break-even point of a staining machine

From *figure 10*, the net production at the break-even point can be seen to be 75.74 times, which is the number of tests needed for the investment to be equal to revenue. To be profitable, the device has to be used to test tissue samples for 76 times and up. When maintenance expenses were included in the variable costs, M was defined as the average maintenance cost per operating cycle. The annual maintenance cost was estimated at USD 109.27, based on monthly maintenance and inspection at USD 9.11 per service. Consequently, the variable cost per unit increased from USD 17.00 to USD 17.30, resulting in a calculated break-even point of 78.03 operating cycles, which was rounded up to 79 cycles.

FOREX Publication
Open Access | Rapid and quality publishing
International Journal of Electrical and Electronics Research (IJEER)
Research Article | Volume 14, Issue 3 | Pages 852-862 | e-ISSN: 2347-470X

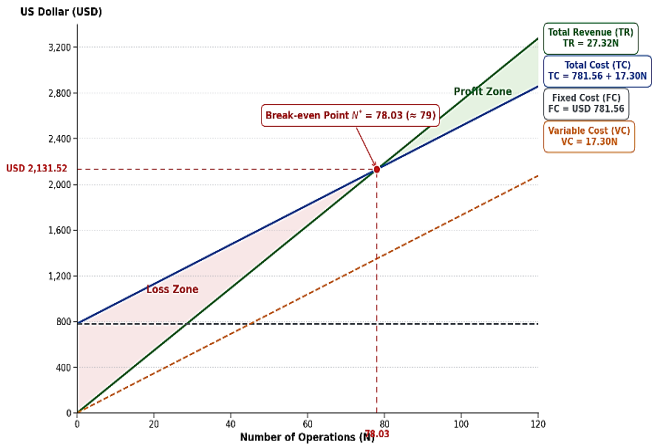


Figure 11. Break-even Point of the Slide Stainer After Maintenance Costs Were Included

As shown in *figure 11*, when maintenance costs were included, the break-even point of the slide-staining machine was 78.03 operating cycles, corresponding to a total revenue of approximately USD 2,131.52. This represented the number of tissue-sample tests required for the total revenue to equal the total investment and operating costs. Therefore, at least 79 tests were required for the machine to generate a profit.

4.8. Results of the Performance Test for Assisting in the Identification of Suspicious Cell Locations

This test evaluates the preliminary performance of the image-processing system in distinguishing images containing suspicious cellular regions from normal images. The evaluation uses 120 images and compares them with the expert-consensus reference standard defined, comprising 48 reference-positive and 72 reference-negative images. A system output is classified as positive when at least one region in the image meets the localization decision rule and as negative when no region is marked. The study compares the image-level system outputs with the consensus labels to obtain True Positives (TP), False Positives (FP), True Negatives (TN), and False Negatives (FN), as shown in *table 7*.

Table 7. Confusion Matrix of Test Results from 120 Images

Actual Result	Predicted Positive	Predicted Negative	Total
Actual Positive	TP = 38	FN = 10	48
Actual Negative	FP = 12	TN = 60	72
Total	50	70	120

According to *table 7*, the system correctly identified 38 images containing suspicious cell regions and correctly classified 60 normal images, while 12 false alarms occurred and the system failed to detect suspicious regions in 10 images. When these results were used to calculate the performance metrics, the outcomes were as shown in *table 8*.

Table 8. Performance Evaluation Results of the Image Processing System

Metric	Formula	Test Result (%)	Estimate (%)	95% CI
Accuracy	(TP + TN) / (TP + TN + FP + FN)	81.67	81.67	73.57–88.14
Sensitivity (Recall)	TP / (TP + FN)	79.17	79.17	65.01–89.53
Specificity	TN / (TN + FP)	83.33	83.33	72.70–91.08
Precision	TP / (TP + FP)	76.00	76.00	61.83–86.94
Negative Predictive Value	TN / (TN + FN)	85.71	85.71	75.29–92.93
F1-score	2TP / (2TP + FP + FN)	77.55	77.55	67.44–85.98
False Positive Rate	FP / (FP + TN)	16.67	16.67	8.92–27.30
False Negative Rate	FN / (FN + TP)	20.83	20.83	10.47–34.99

The system achieves an accuracy of 81.67% (95% CI: 73.57–88.14%), sensitivity of 79.17% (95% CI: 65.01–89.53%), specificity of 83.33% (95% CI: 72.70–91.08%), precision of 76.00% (95% CI: 61.83–86.94%), and F1-score of 77.55% (bootstrap 95% CI: 67.44–85.98%). Fisher's exact test shows a significant association between the reference and system classifications (odds ratio = 19.00, $p < 0.001$). The confidence intervals quantify sampling uncertainty. Because the single-center analysis assumes image-level independence, these results support preliminary screening performance and do not establish clinical diagnostic accuracy.

5. DISCUSSION OF RESEARCH RESULTS

The prototype demonstrates preliminary mechanical reliability: the X-axis completes 10/10 target-position trials, the Y-axis and Z-axis each complete 9/10, and the gripper completes 9/10 operations. The pooled axis reliability is 93.33% (28/30), while the single gripper stall occurs during Z-axis movement. Sliding-rail friction, vertical load, and motor speed or torque settings can explain the Y-axis and Z-axis failures. However, the small number of trials and the absence of millimeter-level endpoint measurements limit conclusions about positioning accuracy. Future validation should use a calibrated displacement gauge and report mean absolute error, standard deviation, maximum error, and long-duration cycle reliability.

The 10-cycle test provides 11.17 h of cumulative operation and shows stable cycle time (67.04 +/- 0.17 min; CV = 0.25%). However, this limited test does not evaluate continuous multi-day operation, maximum 10-slide loading, component wear, reagent degradation, accelerated stress, or recovery after repeated faults. Ambient temperature, humidity, reagent age, and pauses between cycles are not recorded; therefore, the results do not establish long-term endurance or service life.

FOREX Publication
Open Access | Rapid and quality publishing
International Journal of Electrical and Electronics Research (IJEER)
Research Article | Volume 14, Issue 3 | Pages 852-862 | e-ISSN: 2347-470X

On the internal 120-image expert-consensus dataset, the proposed pipeline achieves 81.67% accuracy, 79.17% sensitivity, 83.33% specificity, 76.00% precision, and a 77.55% F1-score. These values provide an internal baseline for this prototype rather than evidence of superiority over other algorithms. The technical novelty does not lie in CLAHE, adaptive thresholding, watershed segmentation, or morphological features individually. It lies in the low-cost system-level integration of automated nine-jar Papanicolaou staining, Raspberry Pi motion control, post-staining image capture, relative within-image thresholds, and an explainable decision rule that localizes regions for expert review without claiming clinical diagnosis.

In terms of economic cost-efficiency, the device had a manufacturing cost of 781.56 USD when compared to 29,777 USD for an imported device, which is a cost reduction of 97.37% with a break-even point at 76 times, reflecting the prototype's capacity for use in laboratories with limited budgets. However, image processing results in this study remained at the level of basic location and insufficient to draw conclusions on clinical diagnostic accuracy.

This study uses only 10 mechanical and repeated-cycle trials under a two-slide load. The evaluation does not include continuous endurance testing, full-load operation, environmental monitoring, wear measurement, or preventive-maintenance intervals. Future work should test at least 100 consecutive cycles at the maximum 10-slide load and report failure count, mean cycles between failures, positioning drift, gripper wear, temperature, humidity, and recovery time.

This study is limited by the number of mechanical test cycles and the single-center dataset of 120 images. Although two qualified assessors establish consensus reference labels, the assessment occurs at the image level and does not include pixel-level boundary annotations, histopathological confirmation, interobserver agreement statistics, or external multicenter validation. Therefore, the reported performance represents preliminary agreement with expert screening judgments rather than clinical diagnostic validity. Future studies should include a larger independently collected dataset, detailed region-level annotations, multiple blinded experts, and external clinical validation.

6. CONCLUSION

This study was aimed at design and development of a low-cost Papanicolaou staining method slide stainer by using Raspberry Pi 4 as the central processing unit for controlling the 3-axis (X, Y, and Z) stepping motors and the servomotor via the slide rack gripper along with displaying results and receiving commands via a 5-inch touch screen display. In addition, this study applied image processing to basically locate cellular anomalies from digital microscope images. Main results are summarized as follows:

Regarding the device's design and creation, the structure was made from 20 x 20-millimeter aluminum profiles with dimensions of 40.0 centimeters in width x 55.0 centimeters in length x 56.0 centimeters in height. The slide stainer supports nine chemical containers and was designed to support a maximum of 10 slides per time. In testing this prototype, two sample slides were used per time. Specific parts, such as the gripper and the stepping motors' base, were designed and manufactured using 3D-printing technology.

In terms of system control, the system was able to start and stop functions via the touch screen display at 100%. The system was able to select work positions with 100% accuracy. Work according to the automated program's sequence had success at 90.00% with one error found out of ten repetitions due to the gripper stalling during movement along the Z axis.

For mechanical operation, the X-axis achieves 100.00% reliability (10/10), while the Y-axis, Z-axis, and gripper each achieve 90.00% (9/10). The pooled axis reliability is 93.33% (28/30), with a 6.67% error rate. These values describe operational repeatability at calibrated target positions; direct millimeter-level positioning error remains to be measured.

The 10-cycle evaluation produces a mean cycle time of 67.04 +/- 0.17 min (CV = 0.25%) and 670.40 min of cumulative operation. The automatic sequence completes 9 of 10 trials. These findings support short-term repeatability only; long-duration endurance under full load remains necessary.

In terms of economic cost-efficiency, the developed slide stainer had a fixed cost of 780 USD, a cost fluctuation of 17USD per time, and revenue at 28USD per time. The break-even point was at 75.74 times or 76 times when rounded up. This is significantly lower than the price of a slide stainer imported from abroad. Image processing was able to basically locate anomalies. However, clinical accuracy needs further clinical verification before application.

In conclusion, the system-level contribution is the integration of low-cost automated nine-jar Papanicolaou staining with a training-free and explainable localization module on one Raspberry Pi platform. The internal results establish a preliminary baseline, not superiority over deep-learning or scanner-based approaches. Further work requires direct testing on a shared external dataset, ablation analysis, region-level annotation, and multicenter clinical validation.

Acknowledgments: This research was supported by the Research Fund of Thailand Science Research and Innovation (TSRI). K.S. also gratefully acknowledges the Faculty of Industrial Technology, Phranakhon Rajabhat University, for their support throughout this study. P.A. gratefully acknowledges the Faculty of Engineering, King Mongkut's University of Technology North Bangkok, for its support of this research. The authors also sincerely appreciate the cooperation and assistance provided by Bhumibol Adulyadej Hospital, Royal Thai Air Force Medical Department, Bangkok, throughout the project.

Conflicts of Interest: The authors declare no conflict of interest.

REFERENCES

[1] Golnabi, H., & Asadpour, A. (2007). Design and application of industrial machine vision systems. Robotics and Computer-Integrated Manufacturing, 23(6), pp. 630–637. https://doi.org/10.1016/j.rcim.2007.02.005

FOREX Publication
Open Access | Rapid and quality publishing
International Journal of Electrical and Electronics Research (IJEER)
Research Article | Volume 14, Issue 3 | Pages 852-862 | e-ISSN: 2347-470X

[2] Farhat, N. & Nasiruddin M. (2022). Computer Vision based Surveillance System. International Journal for Research in Applied Science and Engineering Technology (IJRASET), 10(10), pp. 1491–1494, https://doi.org/10.22214/ijraset.2022.41512

[3] Chung, W., Kim, S., Choi, M., Choi, J., Kim, H., Moon, C., & Song, J. (2009). Safe navigation of a mobile robot considering visibility of environment. IEEE Transactions on Industrial Electronics, 56(10), pp. 3941–3950. https://doi.org/10.1109/TIE.2009.2025293

[4] Channappa, A., Praveena, K. B., & Patrer, D. (2022). IoT-enabled smart surveillance: Adaptive image processing for security applications. World Journal of Advanced Research and Reviews, 15(3), pp. 513–525. https://doi.org/10.30574/wjarr.2022.15.3.0724

[5] Marković, D., Stamenković, Z., Đorđević, B., &Randić, S. (2024). Image processing for smart agriculture applications using cloud-fog computing. Sensors, 24(18), pp. 5965. https://doi.org/10.3390/s24185965

[6] Zhu, N., Liu, X., Liu, Z., Hu, K., Wang, Y., Tan, J., Huang, M., Zhu, Q., Ji, X., Jiang, Y., & Guo, Y. (2018). Deep learning for smart agriculture: Concepts, tools, applications, and opportunities. International Journal of Agricultural and Biological Engineering, 11(4), pp. 32–44. https://doi.org/10.25165/j.ijabe.20181104.4475

[7] Madasamy Raja, G., Deenadhayalan, R., Krishnamoorthy, N., &Anandamurugan, S. (2022). An image processing method for identifying plant diseases based on changes in leaf morphology. Neuro Quantology, 20(9), pp. 2792–2804. https://doi.org/10.14704/nq.2022.20.9.NQ44325

[8] Hu, S., Lu, R., Zhu, Y., Zhu, W., Jiang, H., & Bi, S. (2023). Application of medical image navigation technology in minimally invasive puncture robot. Sensors, 23(16), pp. 7196. https://doi.org/10.3390/s23167196

[9] Li, C., Zhang, G., Zhao, B., Xie, D., Du, H., Duan, X., Hu, Y., & Zhang, L. (2024). Advances of surgical robotics: image-guided classification and application. National Science Review, 11, nwae186. https://doi.org/10.1093/nsr/nwae186

[10] Bhole, M., Bamane, R., Jadhav, R., More, P., & Ture, R. (2021). PLC based object sorting system using image processing. International Journal of Scientific Research in Engineering and Management, 5(5), pp. 1–5.

[11] Farisqi, B. A., & Prahara, A. (2022). Guava fruit detection and classification using mask region-based convolutional neural network. Buletin Ilmiah Sarjana Teknik Elektro, 4(3), pp. 186–193. https://doi.org/10.12928/biste.v4i3.7412

[12] Lawal, O. M., & Zhao, H. (2021). YOLOFig detection model development using deep learning. IET Image Processing, 15(13), pp. 3071–3079. https://doi.org/10.1049/ipr2.12293

[13] Biradar, M. S., Shiparamatti, B. G., & Patil, P. M. (2021). Fabric defect detection using deep convolutional neural network. Optical Memory and Neural Networks, 30(3), 250–256. https://doi.org/10.3103/S1060992X21030024

[14] Biradar, M. S., Sheeparamatti, B. G., & Patil, P. M. (2018). Defect detection and classification in patterned fabric using variational mode image decomposition and neural network. Journal of Emerging Technologies and Innovative Research, 5(10), 769–774. https://www.jetir.org/papers/JETIR1810519.pdf

[15] Alajrami, E., Ashqar, B. A. M., Abu-Nasser, B. S., Khalil, A. J., Musleh, M. M., Barhoom, A. M., & Abu-Naser, S. S. (2019). Handwritten signature verification using deep learning. International Journal of Academic Multidisciplinary Research, 3(12), 39–44. https://www.ijeais.org/ijamr

[16] Sadati Salimi, S. M., Baleghi, Y., & Salehi, E. (2026). Printed circuit board quality control using image processing and modified YOLO structures. International Journal of Engineering, Transactions C: Aspects, 39(9), 2204–2212. https://doi.org/10.5829/ije.2026.39.09c.11

[17] Sheeba, A., Santhosh Kumar, P., Ramamoorthy, M., & Sasikala, S. (2023). Microscopic image analysis in breast cancer detection using ensemble deep learning architectures integrated with web of things. Biomedical Signal Processing and Control, 79, 104048. https://doi.org/10.1016/j.bspc.2022.104048

[18] Zhang, L., Lei, J., Xia, J., & Cai, A. (2022). Diagnostic value of combination of exfoliative cytology with CA125, CEA, NSE, CYFRA21-1 and CA15-3 for lung cancer. Revista Română de Medicină de Laborator, 30(4), 389–398. https://doi.org/10.2478/rrlm-2022-0037

[19] Koss, L. G., & Melamed, M. R. (2006). Koss' diagnostic cytology and its histopathologic bases (5th ed.). Lippincott Williams & Wilkins.

[20] Goel, G., Halder, A., Joshi, D., Anil, A. C., & Kapoor, N. (2020). Rapid, Economic, Acetic Acid Papanicolaou Stain (REAP): An economical, rapid, and appropriate substitute to conventional pap stain for staining cervical smears. Journal of Cytology, 37(4), 170–173. https://doi.org/10.4103/JOC.JOC_89_20

[21] Liao, C., Gong, Z., Fang, R., Li, L., Gao, Z., Mao, M., & Zeng, L. (2024). Design and implementation of corrosion-resistant multitasking cell stainers. PLOS ONE, 19(10), e0309334. https://doi.org/10.1371/journal.pone.0309334

[22] Ocampo-López-Escalera, J., Ochoa-Díaz-López, H., Sánchez-Chino, X. M., Irecta-Nájera, C. A., Tobar-Alas, S. D., & Rosete-Aguilar, M. (2025). A low-cost platform for automated cervical cytology: Addressing health and socioeconomic challenges in low-resource settings. Frontiers in Medical Technology, 7, 1531817. https://doi.org/10.3389/fmedt.2025.1531817

[23] Lu, Q., Liu, G., Xiao, C., Hu, C., Zhang, S., Xu, R. X., Chu, K., Xu, Q., & Smith, Z. J. (2018). A modular, open-source, slide-scanning microscope for diagnostic applications in resource-constrained settings. PLOS ONE, 13(3), e0194063. https://doi.org/10.1371/journal.pone.0194063

[24] Aramnet, C. (2026, March 16). Cancer statistics 2026: Lung cancer is the number one killer. Bangkok Biz News. https://www.bangkokbiznews.com/health/well-being/1225390

[25] Suvarna, S. K., Layton, C., & Bancroft, J. D. (2012). Bancroft's theory and practice of histological techniques (7th ed.). Churchill Livingstone Elsevier.

[26] Schulte, E. (1990). Standardization of the Papanicolaou stain. I. A comparison of five nuclear stains. Analytical and Quantitative Cytology and Histology, 12(3), 149–156. https://pubmed.ncbi.nlm.nih.gov/1695100/

[27] Bhanvadia, V. M., Santwani, P. M., & Vachhani, J. H. (2014). Analysis of diagnostic value of cytological smear method versus cell block method in body fluid cytology: Study of 150 cases. Ethiopian Journal of Health Sciences, 24(2), 125–131. http://dx.doi.org/10.4314/ejhs.v24i2.4

[28] Ponzetti, M., Devarapu, G. C. R., Rucci, N., Carlone, A., & Saggiomo, V. (2022). HistoEnder: A 3D printer-based histological slide autostainer that retains 3D printer functions. HardwareX, 12, e00370. https://doi.org/10.1016/j.ohx.2022.e00370

[29] Blank, L., & Tarquin, A. (2012). Engineering economy (7th ed.). McGraw-Hill.

[30] Sullivan, W. G., Wicks, E. M., & Koelling, C. P. (2012). Engineering economy (15th ed.). Pearson Education.

© 2026 by the Keeradit Saipattalung, Surasee Prahmkaew, and Pasura Aungkulanon. Submitted for possible open access publication under the terms and conditions of the Creative Commons Attribution (CC BY) license (http://creativecommons.org/licenses/by/4.0/).